

www.acsnano.org

# Inhomogeneous Quantized Single-Electron Charging and Electrochemical—Optical Insights on Transition-Sized Atomically Precise Gold Nanoclusters

Shuang Chen, <sup>⊥</sup> Tatsuya Higaki, <sup>⊥</sup> Hedi Ma, <sup>⊥</sup> Manzhou Zhu, Rongchao Jin,\* and Gangli Wang\*



Cite This: ACS Nano 2020, 14, 16781–16790



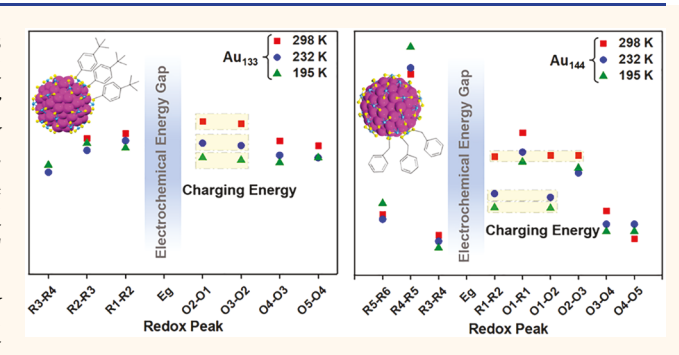
**ACCESS** 

Metrics & More

Article Recommendations

Supporting Information

ABSTRACT: Small differences in electronic structures, such as an emerging energy band gaps or the splitting of degenerated orbitals, are very challenging to resolve but important for nanomaterials properties. A signature electrochemical property called quantized double layer charging, i.e., "continuous" one-electron transfers (1e, ETs), in atomically precise Au<sub>133</sub>(TBBT)<sub>52</sub>, Au<sub>144</sub>(BM)<sub>60</sub>, and Au<sub>279</sub>(TBBT)<sub>84</sub> is analyzed to reveal the nonmetallic to metallic transitions (whereas TBBT is 4-tert-butylbenzenethiol and BM is benzyl mercaptan; abbreviated as Au<sub>133</sub>, Au<sub>144</sub>, and Au<sub>279</sub>). Subhundred milli-eV energy differences are resolved among the "often-approximated uniform" peak spacings from multipairs of reversible redox



peaks in voltammetric analysis, with single ETs as internal standards for calibration and under temperature variations. Cyclic and differential pulse voltammetry experiments reveal a 0.15 eV energy gap for Au<sub>133</sub> and a 0.17 eV gap for Au<sub>144</sub> at 298 K. Au<sub>279</sub> is confirmed metallic, displaying a "bulk-continuum" charging response without an energy gap. The energy gaps and double layer capacitances of Au<sub>133</sub> and Au<sub>144</sub> increase as the temperature decreases. The temperature dependences of charging energies and HOMO–LUMO gaps of Au<sub>133</sub> and Au<sub>144</sub> are attributed to the counterion permeation and the steric hindrance of ligand, as well as their molecular compositions. With the subtle energy differences resolved, spectroelectrochemistry features of Au<sub>133</sub> and Au<sub>144</sub> are compared with ultrafast spectroscopy to demonstrate a generalizable analysis approach to correlate steady-state and transient energy diagram for the energy-in processes. Electrochemiluminescence (ECL), one of the energy-out processes after the charge transfer reactions, is reported for the three samples. The ECL intensity of Au<sub>279</sub> is negligible, whereas the ECLs of Au<sub>133</sub> and Au<sub>144</sub> are relatively stronger and observable (but orders of magnitudes weaker than our recently reported bimetallic Au<sub>12</sub>Ag<sub>13</sub>). Results from these atomically precise nanoclusters also demonstrate that the combined voltammetric and spectroscopic analyses, together with temperature variations, are powerful tools to reveal subtle differences and gain insights otherwise inaccessible in other nanomaterials.

**KEYWORDS:** nanoclusters, quantized double layer (QDL) charging, spectroelectrochemistry, ultrafast, electrochemiluminescence (ECL), charging energy, energy gap

etal nanoclusters (NCs) differ from regular nanoparticles with ultrasmall sizes and thus more prominent quantum effects, and with definitive atomic compositions and structures built on recent advances in the syntheses and characterizations. From the perspective of properties, one might argue that the existence of an energy band gap would be a more fundamental and quantitative descriptor for metal nanoclusters over larger nanomaterials of the same metal. Whether a band gap exists and how it is dependent on the composition/structure are fundamentally significant and have broad implications to various electro-

chemical, optical, and other properties. However, determining small energy differences and how the energy states change under reaction conditions, especially in the transition-size

Received: June 12, 2020 Accepted: November 10, 2020 Published: November 16, 2020





range from nanoclusters to larger nanomaterials, is challenging experimentally.

Electrochemical techniques are intrinsically suitable to measure charge transfers and related energy states/orbitals by direct oxidation or reduction at a specific orbital/energy state via electrode reactions. Resolving small energy differences in transition-sized nanoclusters, however, is complicated by a signature electrochemical behavior called quantized double layer (QDL) charging initially observed from Au nanoclusters. 5,6 The Au nanoclusters are the most studied prototype, also referred to as monolayer protected clusters (MPCs) in earlier literature, which are composed of an Au core stabilized by a monolayer of thiolate ligands.<sup>3,7,8</sup> The QDL results from continuous or multiple one-electron transfer reactions (1e ETs) when the nanoclusters are considered as nanosized capacitors. With the capacitance in the atto-Farad range depending on the core and ligands, the charging energy needed for 1e ETs would be constant (at about hundred(s) of milli-eV) assuming that the capacitance remains constant, and thus display "uniformly spaced" peaks in current-potential plots. 9-11 Although inhomogeneity in QDL peak spacing was noticed long ago, significant insight such as the existence of small energy gap(s) could not be determined due to the previously inevitable sample polydispersity, which causes the capacitance and thus the charging energy to vary. 12-14 Therefore, atomically precise NCs are critically needed in order to gain insights into the fine features of QDL.

Unlike pure metals or naked clusters, ligand effects on the overall energy diagram can no longer be ignored especially when ligands are covalently attached to metal cores in nanoclusters. 15-20 An exemplary case is the significant contributions from sulfur atomic orbitals to the energy states of Au-thiolate clusters revealed by superatom theory. 20,21 In general, the energy gap increases with the decrease in size, though it also depends on atomic structures. Currently, discrepancies in the literature dispute such a trend of monotonous dependence in the nonmetal to metal transition range. Au<sub>246</sub>(p-MBT)<sub>80</sub> is shown to be the largest nonmetallic nanocluster in the quantum size regime to date, whereas Au<sub>329</sub>(PET)<sub>84</sub> is found to have no obvious electrochemical gap and being metallic.<sup>22-24</sup> Furthermore, Au<sub>279</sub> (TBBT)<sub>84</sub> is determined to be metallic by transient absorption spectroscopy but electrochemistry analysis is still absent. 25,26 An abnormal case is the electrochemical properties of Au<sub>133</sub>(TBBT)<sub>52</sub> reported by Dass and co-workers, in which no electrochemical energy gap in Au<sub>133</sub> was identified.<sup>27</sup> The same report analyzed Au<sub>144</sub>(PET)<sub>60</sub> and showed a clear ~0.37 V peak spacing.<sup>27</sup> Theoretical analyses on  $Au_{144}$  and similar-sized  $Au_{146}$  also showed small gaps. <sup>29,30</sup> Further, the similar-sized  $Au_{130}$  exhibits a clear ~0.45 and 0.50 V voltammetric peak spacing with monothiol ligands<sup>31,32</sup> and ~0.35 V with mixed mono- and dithiol ligands in earlier work.<sup>33</sup> With the increasing availability of atomic structures and compositions of nanoclusters, density functional theory calculations provide energy diagrams with great detail; meanwhile, experimental probing and confirmation of theory would be highly desirable, ideally in both energy levels and density of states, at least semiquantitatively.<sup>34</sup> Electrochemical characterizations at subhundred milli-eV, the energy range of electronic transitions overlapping with nuclear vibrations, remain scarce and challenging. The correlation and validation of energy diagram with structures in the nanoclusterto-nanoparticle transition regime would provide much needed

guidance on the design and development of the fast-growing atomically precise nanoclusters and other relevant materials.

In this report, well-defined  $Au_{133}$ ,  $Au_{144}$ , and  $Au_{279}$  NCs (atomic structures shown in Figure 1, steady-state UV-visible

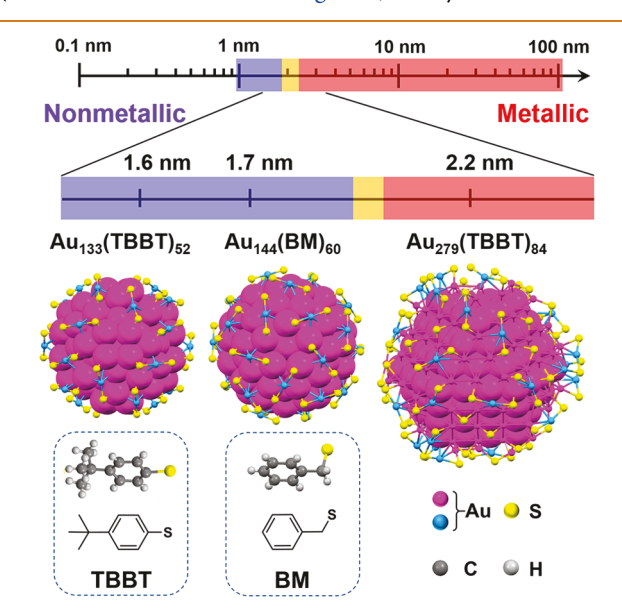


Figure 1. Structures of  $Au_{133}$ ,  $Au_{144}$ , and  $Au_{279}$  and size transition from nonmetallic molecule-like to metallic nanoparticles.

absorption spectra in Supporting Information Figure S1) are chosen to demonstrate how to achieve subhundred milli-eV resolution in electrochemical analysis, to reconcile the apparent discrepancy in the qualitative trend of the transition from molecular-like nanoclusters with discrete orbitals to larger nanoparticles with band structure, and to demonstrate a generalizable approach to correlate steady-state and transient spectroscopic features under related charge transfer conditions.

### **RESULTS AND DISCUSSION**

Basic Voltammetry Features. Electrochemical properties of the Au<sub>133</sub>, Au<sub>144</sub>, and Au<sub>279</sub> NCs characterized by cyclic and differential pulse voltammetry (CV and DPV) are summarized in Figure 2. Twelve pairs of quantized double layer (QDL) charging peaks are identified in Au<sub>133</sub>. The consistent 59 mV potential difference between each pair of reduction and oxidation QDL peaks indicate facile and reversible electron transfer (ET) for the core charging/discharging activities. In other words, the Au NCs are chemically stable and the corresponding energy states are not shifted upon the ET reaction. The ET reversibility is further confirmed by the independence of peak positions at higher scan rates shown in Figure S2. In Au<sub>144</sub>, about 13 pairs of QDL redox peaks are observed in the mid-potential range. Toward more negative potentials, the cathodic CV current at above -1 V is much higher than the one-electron QDL current (about 8 times herein). Though under thorough purging and stringent controls for consistency in analyzing different samples, residual oxygen might still contribute to this current and affect the quantitation. Similar to the Au<sub>133</sub>, the reversible ET of this QDL charging is confirmed by the consistent 60 mV peak separations of each redox pair that remain unchanged at higher scan rates (Figure S3). The CV of Au<sub>279</sub> is smooth and featureless, as opposed to the stepwise quantized one-electron QDL charging in the two smaller NCs. The two current

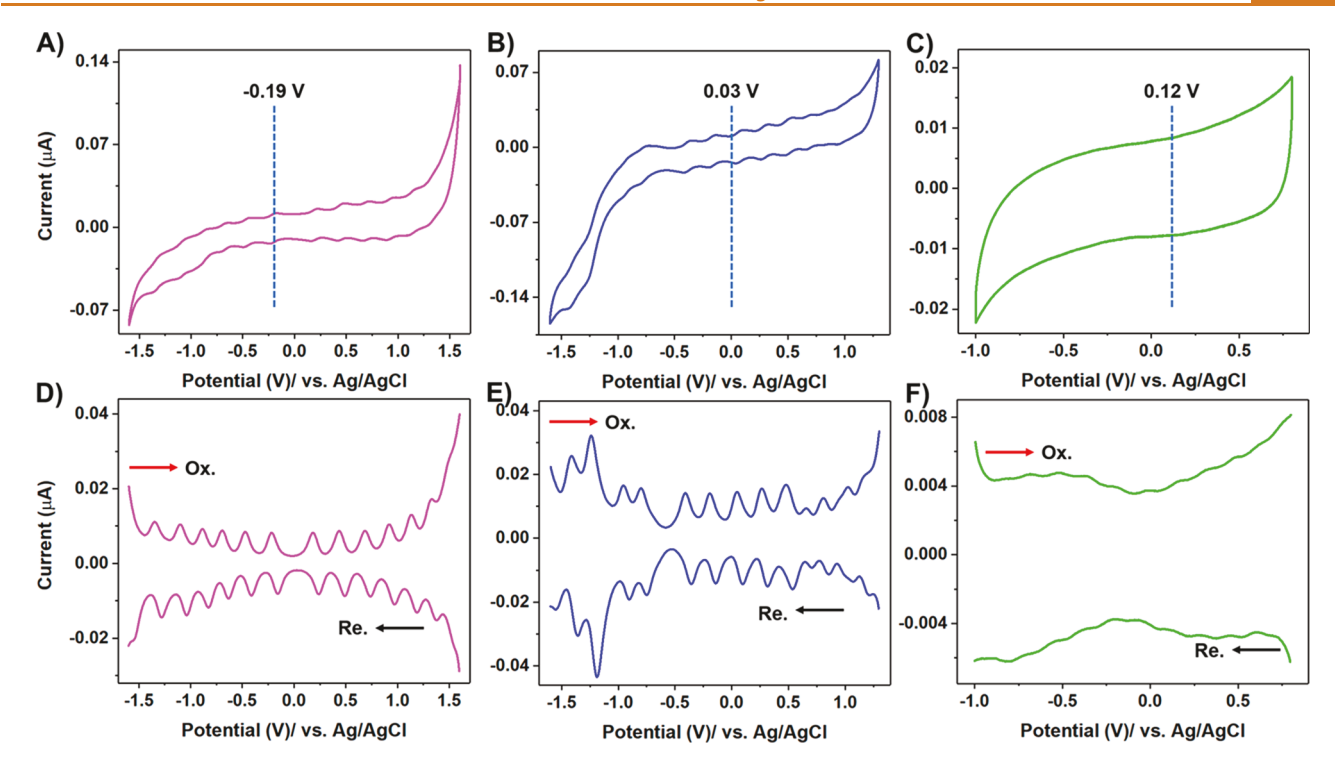


Figure 2. CVs (A–C) and DPVs (D–F) of  $Au_{133}$  (A and D, pink lines),  $Au_{144}$  (B and E, blue lines), and  $Au_{279}$  (C and F, green lines). The concentration of Au NCs is  $ca. \sim 1$  mM in DCM with 0.1 M TBAP (tetra-n-butylammonium perchlorate). The potential scan rate in CV is 0.1 V/s. All experiments were performed at 298 K except for the DPV of  $Au_{279}$  that is at 232 K. Red arrows are oxidation scans, and black arrows are reduction scans in DPVs. The dashed lines indicate the rest potentials of  $Au_{133}$ ,  $Au_{144}$ , and  $Au_{279}$  at -0.19, 0.03, and 0.12 V, respectively.

branches are largely in parallel, which is characteristic of normal capacitive charging, or "bulk-continuum" (double layer) capacitor behaviors. The "bulk" nature of Au<sub>279</sub> is qualitatively consistent with the concentric sphere model in which a large core or capacitance would cause the peak spacing or charging energy to decrease, and thus harder to resolve experimentally. The stability of all three NCs during the voltammetric measurements is also supported by the insignificant changes in the UV—vis absorption spectra before and after the voltammetric measurements (Figure S4).

Differentiating Charging Energy from Different Energy States or Shift/Splitting. The peak positions and minor irregularities among the peak spacing  $(\Delta V)$  are better resolved in the corresponding DPV results. The  $\Delta V$  values determined from both oxidation and reduction DPVs are highly consistent (within about  $\pm 4$  mV) listed in Table S1. For Au<sub>133</sub>, a much larger 0.40<sub>0</sub> V gap is clearly discernible, between the oxidation and reduction peaks at 0.184 V (O1) and -0.216 V (R1), among the otherwise more uniform peak spacings. As for Au<sub>144</sub>, two pairs of cathodic peaks can be seen at around -1.2 and -0.8 V, separated by a  $0.39_1$  V gap from five highly uniform QDL peaks on the positive direction. QDL (10 pairs) features can only be resolved from the Au<sub>279</sub> at lower temperature (232 K) by DPV explained further below. The peak spacing  $\Delta V$ s are highly uniform ( $\Delta V$ s in the range of 0.16<sub>4</sub>-0.17<sub>4</sub> V). Although single millivolt resolution can be read from the measured data, the subten mV difference is within the broadening by Boltzmann distribution and further limited by the pulse height (50 mV). In other words, the energy gap (if any) of Au<sub>279</sub> cannot be determined from these electrochemical analyses.

Next, we scrutinize the irregularities in the peaking spacing  $\Delta Vs$  to resolve different energy states. By identifying more

uniform  $\Delta V$  or charging energy as internal standard, a resolution of lower tens milli-eV can be achieved to differentiate energy states/orbitals because thermal agitation and other measurement limitations are the same within a data set. The DPVs of  $\mathrm{Au}_{133}$  and  $\mathrm{Au}_{144}$  collected at different temperatures are analyzed in Figure 3. The subtle differences among  $\Delta V$ s and their temperature dependence are revealed in panels B and D by excluding the much larger  $\Delta V$  of 0.39–0.40 V. This electrochemical gap is attributed to the energy gap between "HOMO–LUMO" frontier states plus charging energy.

In  $Au_{133}$ , the peak spacing  $\Delta V$  displays a parabolic shape from the energy gap toward higher potentials (positive and negative), corresponding to the gradual and slight decrease in charging energy in more oxidized/reduced states (Figure 3B and Figure S5). The trend is consistent with the counterion permeation model in which permeation or intercalation of electrolyte ions would increase the relative permittivity of the ligand monolayer and thus the QDL compact capacitance  $(C = 4\pi\varepsilon_0 \varepsilon^{\frac{r(r+d)}{d}})$ , where  $\varepsilon$  is the dielectric constant or relative permittivity of the dielectric layer of a capacitor, i.e., the ligand monolayer;  $\varepsilon_0$  the permittivity of free space; and r the core radius and d the monolayer thickness). For one-electron transfer processes, the double layer capacitances ( $C_{CLU}$ ) is correlated to the peak spacing  $\Delta V$  and unit charge e by the equation:  $\Delta V = e/C_{\text{CLU}}$ . The smaller  $\Delta V_{\text{S}}$  at lower temperatures correspond to an increase in QDL capacitance which is explained by the increase in the  $\varepsilon$  of hydrocarbon monolayer ("oil"). Also shown in the individual temperature plots in Figure S5, the parabola shape flattens at lower temperature and can no longer be resolved at 195 K. The phenomenon is explained by the weakened ion/solvent

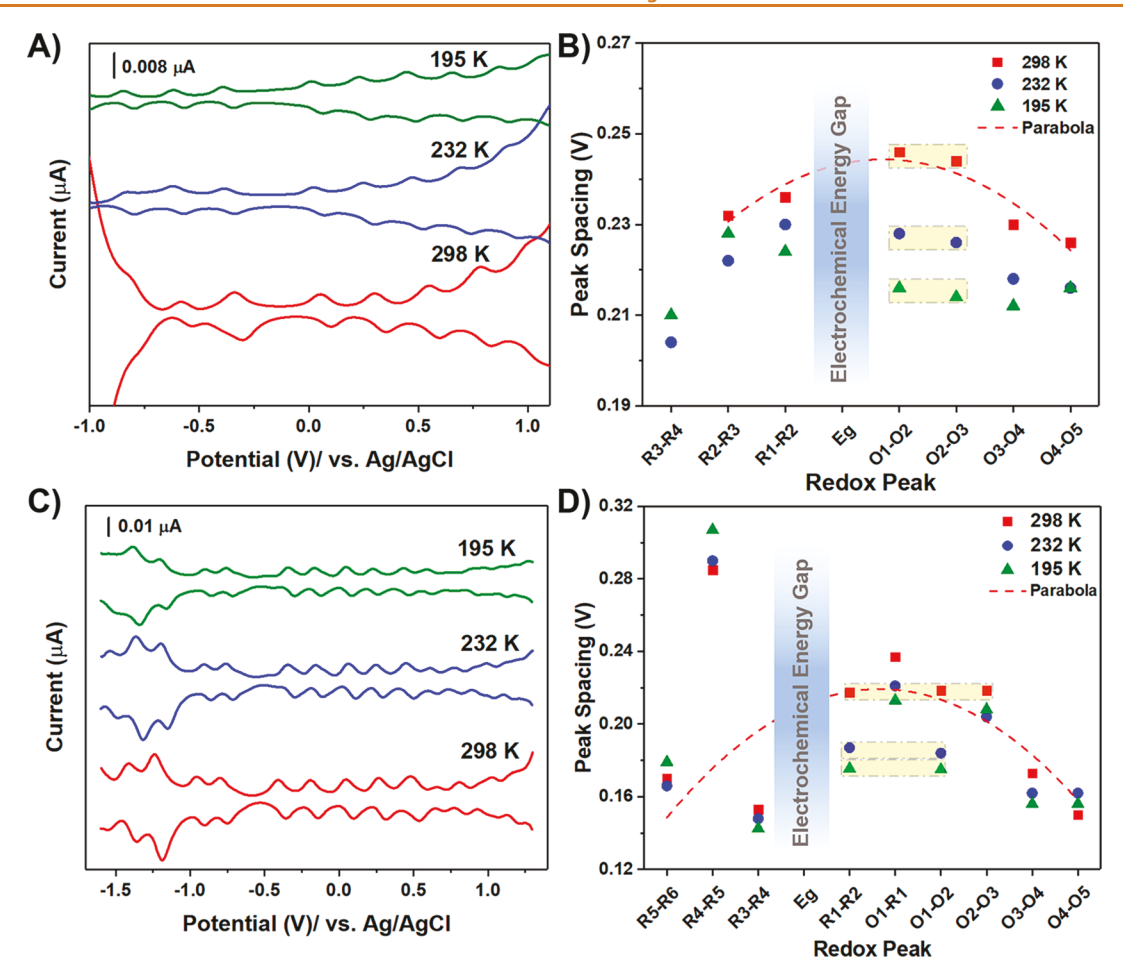


Figure 3. Temperature dependence of electrochemical properties of  $Au_{133}$  and  $Au_{144}$ . The DPVs of (A)  $Au_{133}$  and (C)  $Au_{144}$  at 298, 232, and 195 K. Peak spacing  $\Delta Vs$  analyzed (B and D), respectively.

permeation, i.e., decreased molecular motion at lower temperatures

Interestingly, the charging energy is much less sensitive to temperature variations in the reduced states versus the oxidized Au<sub>133</sub> NCs. Given the  $\varepsilon$  of hydrocarbon monolayer being a function of ligand numbers, ligand molecular structures determining the conductivity and dielectric layer thickness (d), and ion/solvent permeation/intercalation etc., we attribute the asymmetric response (oxidation versus reduction) to the steric hindrance on counterion permeation: the tetrabutylammonium cations are a lot bulkier than perchloride anions to access the core stabilized by a bulky tert-butyl terminal functionality. The relatively larger decrease in charging energy of the oxidized NCs at lower temperatures is explained by the compact capacitance changes affected by different extent of solvent/counterion permeation accordingly. The leveling behavior of low oxidation states at lower temperatures (compared to higher oxidation states) seems to suggest a threshold for ion/solvent permeation, which is reasonably expected for a given monolayer "free volume". With less counterion effects in reduced states, the weaker temperature dependence of the charging energy can arise from two factors: the  $\varepsilon$  of hydrocarbon monolayer or the diffuse layer capacitance.14 The results highlight that an accurate discrimination of different energy states at ca. sub-100 meV resolution should use the appropriate charging energy at the specific charge states and conditions, rather than the average values as widely adopted. Accordingly, the average  $\Delta V$  from the points

near the energy gap (Figure 3B and Figure S5, highlighted by yellow rectangle) is adopted as charging energy for the analysis of energy band gap.

The benzyl mercaptan monolayer on Au<sub>144</sub> is thinner without the bulky tert-butyl portion and more flexible with the CH<sub>2</sub> group. With similar core diameter compared to Au<sub>133</sub>, larger capacitance or smaller  $\Delta V$ s are measured as expected. The peak spacing  $\Delta V$ s vary almost in an alternative high-low manner, corresponding to consecutive pairs of redox peaks. The oscillatory pattern suggests small splitting of degenerated orbitals/energy states assuming the charging energy remains constant. Besides the large gap at 0.391 eV, the next notable gap of 0.28-0.32 eV separates a pair of peaks above the energy gap, i.e., "LUMO", from higher energy states. The rest splitting between the highs to the next lows is about 0.04 eV or larger, with values listed in Table S1. The  $\Delta V_s$  at different temperatures display no clear pattern or difference between oxidation versus reduction, suggesting less discrimination against electrolyte ions of this thinner/leak monolayer.<sup>37</sup> Ignoring the oscillatory pattern and the two obvious gaps, a parabolic shape can still be argued centered at the rest potential (0.03 V), instead of between the energy gap in the case of Au<sub>133</sub> (Figure 3D and Figure S6). The results suggest two vacancies in the degenerated HOMO frontier orbital set. Following the trend established in Au<sub>133</sub> and in reference to the  $\Delta Vs$  at higher potentials (O3/O4, O4/O5, and R5/R6), the  $\Delta V$  as highlighted is adopted to charging energy (Figure 3D and Figure S6, highlighted by yellow rectangle) to calculate the

energy gap and to discriminate the splitting of orbitals/states. To further confirm the more complex patterns of the  $Au_{144}$ , the BM ligands were substituted with the bulky TBBM (TBBM is P-tert-butyl benzyl mercaptan) via ligand exchange, which is a nontrivial task. All main redox features are retained, including the two gaps and the oscillatory  $\Delta Vs$  (Figures S7–S9). The determined charging energy is about 30 meV higher consistently with the added tert-butyl layer at each temperature, which gives a larger monolayer thickness and thus smaller capacitance or slightly larger  $\Delta Vs$ . However, the discrimination of counterions, cations upon oxidation and anions upon reduction, was not as obvious compared to  $Au_{133}$ . Apparently the extra  $CH_2$  group in TBBM made the monolayer more flexible and leaker than TBBT ones.

The highly uniform samples allow us to interpret the irregularities in the  $\Delta V$ s at resolution. The broadening effects by Boltzmann distribution can be evaluated by the width of half-maximum  $(W_{1/2})$  of DPV peaks following the equation for the one-electron process:  $W_{1/2} = 3.52RT/F$ , where R is the gas constant and  $\vec{F}$  the Faraday constant.  $W_{1/2}$  is predicted theoretically to be 90, 70, and 62 mV at 298, 232, and 195 K, respectively, though practical parameters such as pulse height (50 mV) can further broaden the redox peaks and lower the resolution. While baseline separation is not necessary in DPV to determine the peak positions, a value larger than one for the parameter of  $\Delta V/2W_{1/2}$ , that being the resolution between two neighboring peaks with comparable  $W_{1/2}$ , confirms the accurate determination of the peak spacings. From the experimentally measured  $W_{1/2}$  at different temperatures (Table S2), any irregularities more than 20-30 mV can be resolved to reflect the properties of the sample.

**Energy Gap between Frontier Orbitals/States.** The values of charging energy used, the calculated capacitance, and energy gap are listed in Table 1. Those results at different

Table 1. Electrochemical Characterizations of  $Au_{133}$  and  $Au_{144}$  at 298, 232, and 195  $K^a$ 

Temp. (K)	$\frac{\Delta V}{(\mathrm{V})}$	$C_{\mathrm{CLU}}$ (aF)	$\lnC_{\rm CLU}$	$E_{\rm g}$ (V)	HOMO-LUMO gap (eV)
			Au <sub>133</sub>		
298	0.246	0.65	-0.43	$0.40_{0}$	0.154
232	$0.22_{8}$	0.70	-0.36	0.408	0.18 <sub>0</sub>
195	0.216	0.74	-0.30	$0.40_{8}$	0.192
			$Au_{144}$		
298	0.218	0.73	-0.31	$0.39_{1}$	0.17 <sub>3</sub>
232	$0.18_{5}$	0.86	-0.15	0.416	0.231
195	$0.17_{7}$	0.90	-0.11	0.414	0.237

"The single mV digit is listed to demonstrate the uncertainty of the calculated capacitance and band gap (one less significant figures).  $\Delta V$  is the appropriate peak spacing determined from Figure 3,  $C_{\rm CLU}$  is the double layer capacitance, and  $E_{\rm g}$  is the electrochemical energy gap (HOMO-LUMO gap plus  $\Delta V$ ).

temperatures from the two samples, though not large, are statistically different. Of note, no electrochemical gap was resolved/claimed for the same Au<sub>133</sub> in the earlier report by Dass and co-workers, likely from either slight variation in sample quality or the less scrutinization on the inhomogeneous charging energy.<sup>27</sup> The HOMO–LUMO gap of Au<sub>144</sub> is larger than that of Au<sub>133</sub>, 0.17<sub>3</sub> eV *versus* 0.15<sub>4</sub> eV at room temperature. The difference increases at lower temperatures, to 0.23<sub>7</sub> eV *versus* 0.19<sub>2</sub> eV or 45 meV at 195 K. Qualitatively speaking, larger Au cores would correspond to smaller band

gaps. In reference to other  $\mathrm{Au_{130/3}}$  NCs and  $\mathrm{Au_{144/6}}$  NCs,  $^{27,39-41}$  the hollow center in the core atomic structure of  $\mathrm{Au_{144}}$  is believed responsible for the larger HOMO–LUMO gap of  $\mathrm{Au_{144}}$ . It is logical to perform similar analysis on  $\mathrm{Au_{246}}$ , another nonmetallic NC and smaller than  $\mathrm{Au_{279}}$ .  $\mathrm{22,223,25,26}$  DPV results at varied temperatures (Figure S10) confirm its nondetectable energy gap, as well as diminished yet distinguishable trends in charging energy such as (1) a parabolic shape with respect to the applied potential and (2) decrease and leveling at lower temperatures and higher potentials. No detectable energy gap or trends in charging energy were resolved from the larger  $\mathrm{Au_{279}}$  (results not shown).

The enthalpy and entropy portions in the Gibbs free energy changes associated with the electron transfer reaction of  $Au_{133}$  and  $Au_{144}$  can be estimated from the intercept and slope of the linear fitting of HOMO–LUMO gap at different temperatures. In Figure 4, both the extrapolated intercept and the slope are

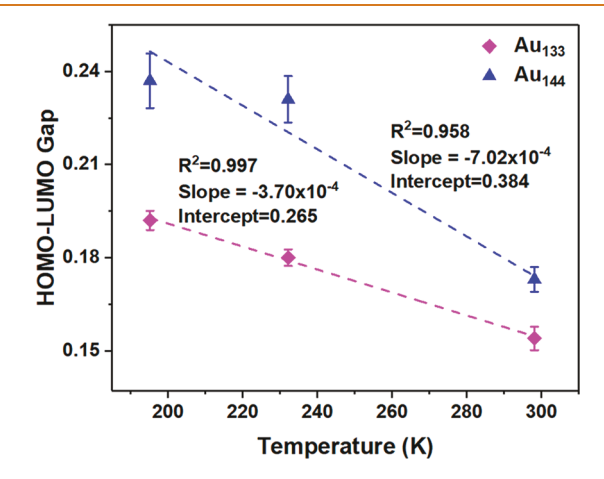


Figure 4. HOMO-LUMO gaps of  $Au_{133}$  (pink) and  $Au_{144}$  (blue) at 298, 232, and 195 K. Dashed lines are fitting. The error bar represents the standard deviation of the average charging energy highlighted in Figure 3.

larger for Au<sub>144</sub> over Au<sub>133</sub>. The higher enthalpy is attributed to the structure differences in Au<sub>144</sub>. The more sensitive temperature dependence indicates larger entropy which is explained by the more flexible monolayer: short flexible BM ligands without tert-butyl group and thus less steric effect, and slightly larger ligand-to-metal ratio (60/144 for Au<sub>144</sub> versus 52/133 for  $Au_{133}$ ). It is important to mention that the ion/ solvent permeation should be viewed as a dynamic exchange process between the bulk solution and the monolayer: both the extent/amount and the dynamics will contribute to the measured energy states/parameters and possible shift/splitting after the ET reactions. At lower temperatures, the motion of ligands can be more restricted with a reduced degree of freedom in certain vibration/rotation modes. The counterion/ solvent permeation into the ligand monolayer will be less dynamic and correspondingly more constant relative permittivity of the dielectric layer and thus the capacitance. At higher charge states, similar reduction in the dynamics of counterions will arise due to the stronger electrostatics. The entropy factor will vary accordingly, which explains the lower linearity of the Au<sub>144</sub> results.

Comparisons of Spectroelectrochemistry and Ultrafast Spectroscopy Features. In spectroelectrochemistry, the

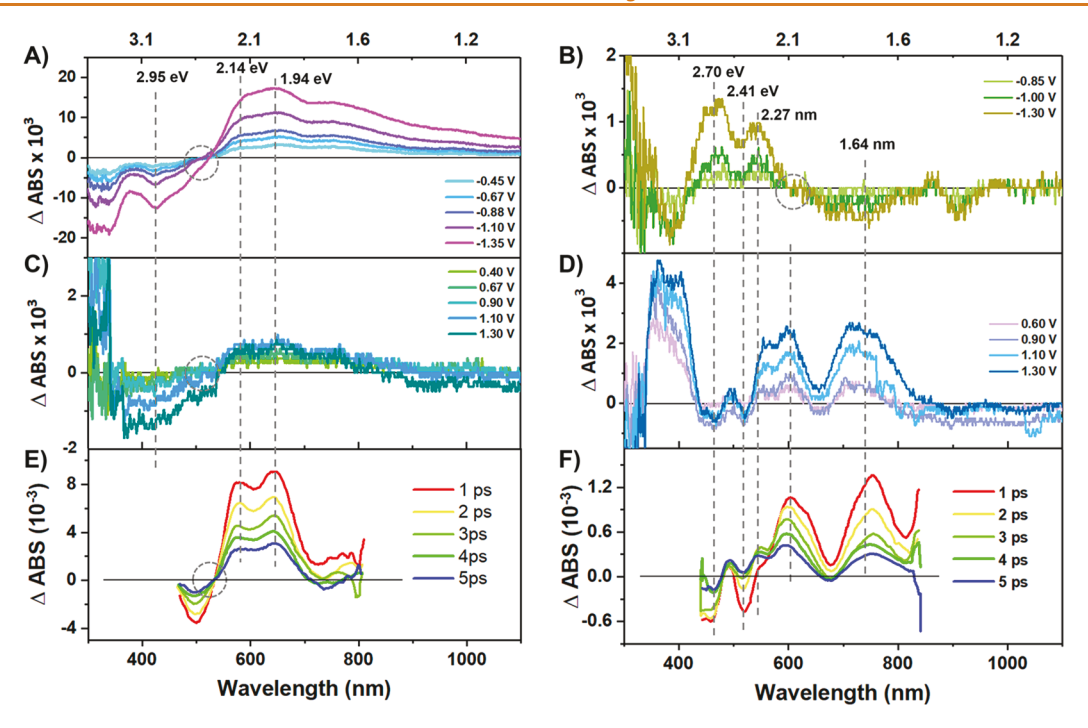


Figure 5. Absorption changes of  $Au_{133}$  (left, A, C, and E) and  $Au_{144}$  (right, B, D, and F) in spectroelectrochemistry and ultrafast spectroscopy.  $\Delta ABS$  calculated by the subtraction with the original spectrum. Panels A and B are after reductive electrolysis and panels C and D after oxidative electrolysis by spectroelectrochemistry. The denoted potentials are the valleys in DPV. Panels E and F are transit absorption spectra. The electronvolts listed above the dashed lines are the distinct absorption bands observed in original steady-state spectra. Additional lines are added to highlight the alignment of key features across different panels.

charge state of the sample is altered directly by addition/ removal of an electron in a particular energy state via electrode ET reactions. The changes in the steady-state absorption spectrum are then collected. The charge states are unchanged in ultrafast spectroscopy; rather, the populations of electrons/ holes in at least two orbitals or energy states are transiently adjusted by a laser and the dynamic changes in spectral features are recorded subsequently. The two techniques can provide complementary insights on energy states and related charge/energy transfer and relaxations, especially when the sample undergoes charge transfer with other entities, as in many applications. The concept and analysis approach are explained by aligning the spectroelectrochemistry results of the Au<sub>133</sub> and Au<sub>144</sub> NCs with previously reported ultrafast data<sup>34,42</sup> in Figure 5. The corresponding original spectra are included in Figures S11-S14 for reference. NCs of these types have been extensively studied, so we defer detailed property discussion to earlier literature and only focus on key comparisons between the two techniques.

The first notion is that spectroelectrochemistry offers information over a much larger energy window (Figure 5, wavelength at the bottom axis and eV energy on the top) with great flexibility and convenience, but lacks dynamics. For example, the distinct 2.95 eV valley in Figure 5A (420 nm peak) and the >3 eV peak in Figure 5D from spectroelectrochemistry are inaccessible in ultrafast mode, which requires highly complex hardware.

Second, the positive or negative  $\Delta ABS$  in spectroelectrochemistry can be correlated to the excited-state absorption (ESA, positive signals) or ground-state bleaching (GSB, negative signals) in ultrafast results but require deliberation. This is because at least two states (unfilled and occupied) are involved in the laser pumping, whereas the electrolysis changes

only one state directly, though indirect changes on other states are inevitable. Of note, a positive  $\Delta ABS$  means an increase in steady-state absorbance after the electrolysis and a one negative for decrease. For example, the 2.14 and 1.94 eV peaks in Figure 5A in spectroelectrochemistry of  $Au_{133}$  match the ESA in ultrafast spectra, and 2.95 eV (420 nm) valley to GSB. For  $Au_{144}$ , the peak around the 1.64 eV absorption band in Figure 5D matches the onset of interband transition from 5d electrons, which will slightly shift due to the ligand effect. The 2.70, 2.41, and 2.27 eV absorption bands (panels B and D) can also find corresponding features in ultrafast spectra (panel F), which mainly originate from the core transitions on the basis of the fast decay. The transition from occupied states across the Fermi energy can contribute to these absorption bands.  $^{34,46,47}$ 

Third, reduction and oxidation electrolysis modify the unoccupied and occupied orbitals respectively and would generate some symmetric/opposite spectral features.<sup>33</sup> While the peak/valley positions reveal the corresponding energy states and possible shifts, the intensity of  $\pm \Delta ABS$  should reflect the accessible density of states (DOS): a lower DOS or number of degenerated orbitals will display stronger changes per one-electron oxidation/reduction. The reduction-induced changes of Au<sub>133</sub> in Figure 5A display the most changes in  $\triangle$ ABS. Key transition features, such as (1) an isosbestic point (circular dotted line) at about 510 nm and (2) the 580 nm (2.14 eV) and 640 nm (1.94 eV) absorption bands, are consistently observed in both techniques. The oxidationinduced  $\Delta ABS$  in Figure 5C is too weak to be reliably interpreted, but the features are under further explorations. For Au<sub>144</sub>, the  $\Delta$ ABS is stronger after oxidation electrolysis (unlike the stronger reduction ones in Au<sub>133</sub>), suggesting stronger perturbation on the frontier occupied

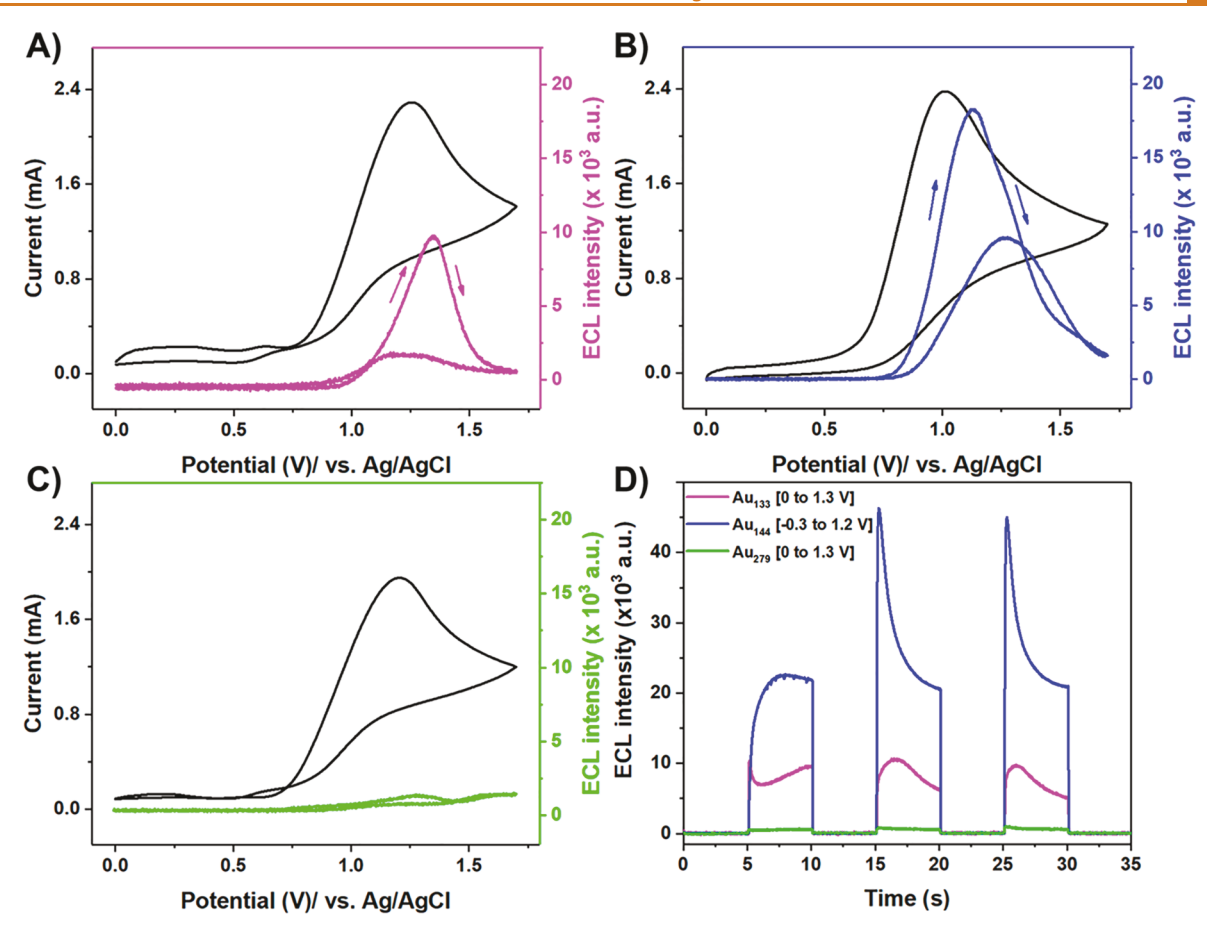


Figure 6. ECL of  $Au_{133}$ ,  $Au_{144}$ , and  $Au_{279}$  under potential scanning (A,  $Au_{133}$ ; B,  $Au_{144}$ ; C,  $Au_{279}$ ) and potential step activations (D). The concentration of  $Au_{133}$ ,  $Au_{144}$ , and  $Au_{279}$  is  $\sim 15 \,\mu\text{M}$  with 0.1 M TBAP electrolyte. The concentration of TPrA co-reactant is 10 mM. Potential scan rate is 0.1 V/s in CV-ECL. The electrode potential is held for 5 s in each step over three cycles at the denoted values.

orbitals. More consistent with previously reported spectroelectrochemistry features, <sup>32,33</sup> oxidation/reduction panels (Figure 5D *versus* Figure 5B) largely mirror each other at respective wavelength ranges qualitatively.

Lastly, irreversible chemical reactions or decomposition could occur in both measurements and affect the analysis. For example, the reduction at high potentials (-1.35~V for  $Au_{133}$  and -1.30~V for  $Au_{144}$ ) induces significant irreversible decompositions. Additional strong changes in absorbance such as the shift in isosbestic point in panel A of Figure 5 should be interpreted in reference to other more consistent features.

Electrogenerated Chemiluminescence or Electrochemiluminescence. In ECL, the excited species are generated by electrode reactions instead of light source. Luminescence occurs when the excess energy, from either oxidation or reduction with optional following reactions, is released via radiative decay. The energy/wavelength and intensity/ efficiency of ECL depends on the energy diagram of the ECL reagents and the ECL reaction pathways (selfannihilation or co-reactants). Figure 6 shows the ECLs from Au<sub>133</sub>, Au<sub>144</sub>, and Au<sub>279</sub> under comparable conditions. Those ECL performances are seven orders of magnitude weaker compared to our recently reported bimetallic Au<sub>12</sub>Ag<sub>13</sub> NCs and not worthy of further explorations. However, ECL is an energy-out measure and much more sensitive over spectroelectrochemistry which analyzes energy-in behaviors. Therefore, combined view of the energy diagram on these three

transition-sized nanoclusters—nanoparticles can be established. With high excess tripropylamine (TPrA) as co-reactants for oxidative—reduction ECL generation, the CV/ECL profiles (panels A–C) and potential step ECLs (D) are compared. The prominent current features such as the oxidation current peak of 1.2 V are dominated by the TPrA co-reactant. While all are weak, the ECL from Au<sub>279</sub> is practically non-exist, which further confirms the continuous electronic energy state or innate metallic character. The trends/comparisons of the weak ECL from these samples are qualitatively comparable to their respective near IR photoluminescence (PL; PL results not shown). In other words, ECL and PL can be potentially used conveniently in a combined or cross-checking fashion to survey or predict high-performing luminophores among the fast-growing list of atomic precise nanoclusters or other materials.

# **CONCLUSION**

In conclusion, energy differences at <0.1 eV resolution under charge transfer conditions are determined in three Au nanoclusters spanning the transition from molecular to metallic state. Discrete energy states in  $\mathrm{Au}_{133}$  and  $\mathrm{Au}_{144}$  nanoclusters and more continuum redox behaviors of metallic  $\mathrm{Au}_{279}$  are revealed by scanning and pulse voltammetric analyses at different temperatures. The voltammetric peak spacing of consecutive one-electron transfer reactions, corresponding to the charging energy (eV), is shown inhomogeneous and depends on measurement conditions. Viewed as nanocapacitors described by concentric sphere model, major

differences in the charging energy (midtens of milli-eV) and the variations upon charge transfer reactions are explained by the changes in compact capacitance due to counterion permeation. The more rigid and thicker ligand monolayer on Au<sub>133</sub> imposes stronger steric hindrance toward bulkier counterions, therefore less changes in relative permittivity and thus double layer capacitance or charging energy. The discrimination of subtle energy differences is achieved by using appropriate charging energy under the respective conditions as internal standard. A 0.154 eV HOMO-LUMO gap in Au133 is determined after the correction of 0.246 eV charging energy, while a 0.173 eV gap above the highest occupied frontier orbitals is observed in Au<sub>144</sub>. The gaps and capacitance of Au<sub>133</sub> and Au<sub>144</sub> increase as the temperature decreases, which reveal the respective enthalpy and entropy contributions to the Gibbs free energy. Optical electronic transitions after electrolysis explored by spectroelectrochemistry are compared to ultrafast spectra. Similarities and differences between the two techniques are discussed to demonstrate a combined approach to analyze steady-state and transient spectral features under charge transfer conditions. ECL of these transition-sized nanoclusters is weak to be of direct practical use alone, but qualitative trends for strong ECL generation such as larger gap or less nonradiative decay pathways can be argued by comparing the ECLsfrom different nanoclusters. Approaches to resolve the subtle energy differences and density of states, and to gain combined electrospectroscopic understanding of the energy-in and energy-out processes under reaction conditions, are believed important to the explorations of the relative physicochemical properties on other nanoclusters or nanomaterials.

# **EXPERIMENTAL SECTION**

**Synthesis.** The syntheses of transition-sized gold nanoparticles (*i.e.*, Au<sub>133</sub>, Au<sub>144</sub>, Au<sub>246</sub>, and Au<sub>279</sub>) were based on size-focusing protocols following reported procedures (details in the Supporting Information). Figure S1 shows the steady-state UV—visible absorption spectra of these three nanoparticles. Au<sub>133</sub> shows three peaks of 420, 510, and 700 nm (pink line). Au<sub>144</sub> exhibits 475, 515, and 715 nm absorption peaks (blue line). Au<sub>279</sub> displays a *ca.* 510 nm metallic surface plasmon resonance (SPR) absorption peak (green line). Those absorption features are highly consistent with the earlier reports, confirming the molecular purity needed for the detailed electrochemical analysis in this report. <sup>25,27,42,45</sup>

**Measurements.** Cyclic and differential pulse voltammograms (CVs and DPVs) were recorded with a CHI Instrument (Model 750C). In general, the nanoclusters were dissolved in DCM at about 1 mM concentration with 0.1 M TBAP (tetra-n-butylammonium perchlorate) as supporting electrolyte. A Pt disk electrode ( $d \sim 0.5$  mm) as working electrode, and an Ag/AgCl wire and Pt foil as reference and counter electrodes were used. A 20 min purging with argon processing was executed before each measurement. Dry ice in ACN and EtOH was used to maintain the test temperature at 232 and 195 K, respectively.

Spectroelectrochemistry and electrochemiluminescence experiments were performed with a three-electrodes system in a quartz cuvette. A Pt mesh working electrode and cuvette were aligned at a fixed position with respect to the detector/camera for consistency. An Ag/AgCl wire as reference electrode and a Pt foil as counter electrode were used (away from a light path). A Dropsens  $\mu$ stat200 benchtop potentiostat and Shimazu UV1700 UV–visible spectrometer were used for spectroelectrochemistry. The ECL emission intensity was recorded with an Andor iDUS CCD camera (Model DU401A-BR-DD). The camera was externally triggered by the potentiostat (Gamry R600) for synchronized light-current detection. The sample solution was purged for about 20 min with argon prior to the measurements.

## **ASSOCIATED CONTENT**

# Supporting Information

The Supporting Information is available free of charge at https://pubs.acs.org/doi/10.1021/acsnano.0c04914.

Syntheses details; steady-state UV-vis absorption spectra; CVs at higher scan rates; data tables of voltammogram peak positions, peak spacing, and capacitance; original spectroelectrochemistry spectra (PDF)

## **AUTHOR INFORMATION**

# **Corresponding Authors**

Gangli Wang — Department of Chemistry, Georgia State University, Atlanta, Georgia 30302, United States;
orcid.org/0000-0001-9204-7807; Email: glwang@

gsu.edu

Rongchao Jin — Department of Chemistry, Carnegie Mellon University, Pittsburgh, Pennsylvania 15213, United States; orcid.org/0000-0002-2525-8345; Email: rongchao@andrew.cmu.edu

# **Authors**

Shuang Chen — Institutes of Physical Science and Information Technology, Anhui University, Hefei, Anhui 230601, People's Republic of China; Key Laboratory of Structure and Functional Regulation of Hybrid Materials, Ministry of Education, Anhui University, Hefei 230601, People's Republic of China

Tatsuya Higaki — Department of Chemistry, Carnegie Mellon University, Pittsburgh, Pennsylvania 15213, United States

**Hedi Ma** – Department of Chemistry, Georgia State University, Atlanta, Georgia 30302, United States

Manzhou Zhu — Institutes of Physical Science and Information Technology, Anhui University, Hefei, Anhui 230601, People's Republic of China; Key Laboratory of Structure and Functional Regulation of Hybrid Materials, Ministry of Education, Anhui University, Hefei 230601, People's Republic of China; orcid.org/0000-0002-3068-7160

Complete contact information is available at: https://pubs.acs.org/10.1021/acsnano.0c04914

# **Author Contributions**

<sup>1</sup>S.C., T.H., and H.M. contributed equally to this work.

### Notes

The authors declare no competing financial interest.

## **ACKNOWLEDGMENTS**

G.W. acknowledges the National Science Foundation (NSF) Grant CHE-1610616. R.J. acknowledges financial support from the NSF (Grant DMR-1808675). S.C. acknowledges the financial support from the National Natural Science Foundation of China (Grant 22004001) and the Department of Education of Anhui Province (Grant 2008085QB84).

# **REFERENCES**

(1) Jin, R.; Zeng, C.; Zhou, M.; Chen, Y. Atomically Precise Colloidal Metal Nanoclusters and Nanoparticles: Fundamentals and Opportunities. *Chem. Rev.* **2016**, *116*, 10346–10413.

(2) Chakraborty, I.; Pradeep, T. Atomically Precise Clusters of Noble Metals: Emerging Link between Atoms and Nanoparticles. *Chem. Rev.* **2017**, *117*, 8208–8271.

- (3) Murray, R. W. Nanoelectrochemistry: Metal Nanoparticles, Nanoelectrodes, and Nanopores. *Chem. Rev.* **2008**, *108*, 2688–2720.
- (4) Chen, S.; Ingram, R. S.; Hostetler, M. J.; Pietron, J. J.; Murray, R. W.; Schaaff, T. G.; Khoury, J. T.; Alvarez, M. M.; Whetten, R. L. Gold Nanoelectrodes of Varied Size: Transition to Molecule-Like Charging. *Science* 1998, 280, 2098–2101.
- (5) Hicks, J. F.; Miles, D. T.; Murray, R. W. Quantized Double-Layer Charging of Highly Monodisperse Metal Nanoparticles. *J. Am. Chem. Soc.* **2002**, *124*, 13322–13328.
- (6) Quinn, B. M.; Liljeroth, P.; Ruiz, V.; Laaksonen, T.; Kontturi, K. Electrochemical Resolution of 15 Oxidation States for Monolayer Protected Gold Nanoparticles. J. Am. Chem. Soc. 2003, 125, 6644–6645.
- (7) Kwak, K.; Lee, D. Electrochemistry of Atomically Precise Metal Nanoclusters. *Acc. Chem. Res.* **2019**, *52*, 12–22.
- (8) Kang, X.; Zhu, M. Tailoring the Photoluminescence of Atomically Precise Nanoclusters. *Chem. Soc. Rev.* **2019**, 48, 2422–2457.
- (9) Garcia-Morales, V.; Mafe, S. Monolayer-Protected Metallic Nanoparticles: Limitations of the Concentric Sphere Capacitor Model. J. Phys. Chem. C 2007, 111, 7242–7250.
- (10) Chen, S.; Murray, R. W. Electrochemical Quantized Capacitance Charging of Surface Ensembles of Gold Nanoparticles. *J. Phys. Chem. B* **1999**, *103*, 9996–10000.
- (11) Su, B.; Zhang, M.; Shao, Y.; Girault, H. H. Solvent Effect on Redox Properties of Hexanethiolate Monolayer-Protected Gold Nanoclusters. J. Phys. Chem. B 2006, 110, 21460–21466.
- (12) Miles, D. T.; Murray, R. W. Redox and Double-Layer Charging of Phenothiazine Functionalized Monolayer-Protected Clusters. *Anal. Chem.* **2001**, *73*, 921–929.
- (13) Scanlon, M. D.; Peljo, P.; Mendez, M. A.; Smirnov, E.; Girault, H. H. Charging and Discharging at the Nanoscale: Fermi Level Equilibration of Metallic Nanoparticles. *Chem. Sci.* **2015**, *6*, 2705–2720
- (14) Miles, D. T.; Murray, R. W. Temperature-Dependent Quantized Double Layer Charging of Monolayer-Protected Gold Clusters. *Anal. Chem.* **2003**, *75*, 1251–1257.
- (15) Jiang, D.-e.; Tiago, M. L.; Luo, W.; Dai, S. The "Staple" Motif: A Key to Stability of Thiolate-Protected Gold Nanoclusters. *J. Am. Chem. Soc.* **2008**, *130*, 2777–2779.
- (16) Xu, W. W.; Zhu, B.; Zeng, X. C.; Gao, Y. A Grand Unified Model for Liganded Gold Clusters. *Nat. Commun.* **2016**, *7*, 13574.
- (17) Jadzinsky, P. D.; Calero, G.; Ackerson, C. J.; Bushnell, D. A.; Kornberg, R. D. Structure of A Thiol Monolayer-Protected Gold Nanoparticle at 1.1 Å Resolution. *Science* **2007**, *318*, 430–433.
- (18) Li, J.; Li, X.; Zhai, H.-J.; Wang, L.-S. Au<sub>20</sub>: A Tetrahedral Cluster. *Science* **2003**, 299, 864–867.
- (19) Zhu, M.; Aikens, C. M.; Hollander, F. J.; Schatz, G. C.; Jin, R. Correlating the Crystal Structure of A Thiol-Protected Au<sub>25</sub> Cluster and Optical Properties. *J. Am. Chem. Soc.* **2008**, *130*, 5883–5885.
- (20) Rambukwella, M.; Sakthivel, N. A.; Delcamp, J. H.; Sementa, L.; Fortunelli, A.; Dass, A. Ligand Structure Determines Nanoparticles' Atomic Structure, Metal-Ligand Interface and Properties. *Front. Chem.* **2018**, *6*, 330.
- (21) Walter, M.; Akola, J.; Lopez-Acevedo, O.; Jadzinsky, P. D.; Calero, G.; Ackerson, C. J.; Whetten, R. L.; Gronbeck, H.; Hakkinen, H. A Unified View of Ligand-Protected Gold Clusters as Superatom Complexes. *Proc. Natl. Acad. Sci. U. S. A.* **2008**, *105*, 9157–9162.
- (22) Zeng, C.; Chen, Y.; Kirschbaum, K.; Lambright, K. J.; Jin, R. Emergence of Hierarchical Structural Complexities in Nanoparticles and Their Assembly. *Science* **2016**, *354*, 1580–1584.
- (23) Zhou, M.; Zeng, C.; Song, Y.; Padelford, J. W.; Wang, G.; Sfeir, M. Y.; Higaki, T.; Jin, R. On the Non-Metallicity of 2.2 nm Au<sub>246</sub>(SR)<sub>80</sub> Nanoclusters. *Angew. Chem., Int. Ed.* **2017**, *56*, 16257–16261.
- (24) Dass, A.; Sakthivel, N. A.; Jupally, V. R.; Kumara, C.; Rambukwella, M. Plasmonic Nanomolecules: Electrochemical Resolution of 22 Electronic States in Au<sub>329</sub>(SR)<sub>84</sub>. ACS Energy Lett. **2020**, *5*, 207–214.

- (25) Higaki, T.; Zhou, M.; Lambright, K. J.; Kirschbaum, K.; Sfeir, M. Y.; Jin, R. Sharp Transition from Nonmetallic Au<sub>246</sub> to Metallic Au<sub>279</sub> with Nascent Surface Plasmon Resonance. *J. Am. Chem. Soc.* **2018**, *140*, 5691–5695.
- (26) Sakthivel, N. A.; Theivendran, S.; Ganeshraj, V.; Oliver, A. G.; Dass, A. Crystal Structure of Faradaurate-279: Au<sub>279</sub>(SPh-tBu)<sub>84</sub> Plasmonic Nanocrystal Molecules. *J. Am. Chem. Soc.* **2017**, *139*, 15450–15459.
- (27) Dass, A.; Theivendran, S.; Nimmala, P. R.; Kumara, C.; Jupally, V. R.; Fortunelli, A.; Sementa, L.; Barcaro, G.; Zuo, X.; Noll, B. C. Au<sub>133</sub>(SPh-tBu)<sub>52</sub> Nanomolecules: X-ray Crystallography, Optical, Electrochemical, and Theoretical Analysis. *J. Am. Chem. Soc.* **2015**, 137, 4610–4613.
- (28) Nimmala, P. R.; Theivendran, S.; Barcaro, G.; Sementa, L.; Kumara, C.; Jupally, V. R.; Apra, E.; Stener, M.; Fortunelli, A.; Dass, A. Transformation of Au<sub>144</sub>(SCH<sub>2</sub>CH<sub>2</sub>Ph)<sub>60</sub> to Au<sub>133</sub>(SPh-tBu)<sub>52</sub> Nanomolecules: Theoretical and Experimental Study. *J. Phys. Chem. Lett.* **2015**, *6*, 2134–2139.
- (29) Weissker, H. C.; Lopez-Acevedo, O.; Whetten, R. L.; López-Lozano, X. Optical Spectra of the Special Au<sub>144</sub> Gold-Cluster Compounds: Sensitivity to Structure and Symmetry. *J. Phys. Chem.* C 2015, 119, 11250–11259.
- (30) López-Lozano, X.; Plascencia-Villa, G.; Calero, G.; Whetten, R. L.; Weissker, H.-C. Is the Largest Aqueous Gold Cluster A Superatom Complex? Electronic Structure & Optical Response of the Structurally Determined Au<sub>146</sub>(p-MBA)<sub>57</sub>. *Nanoscale* **2017**, *9*, 18629–18634.
- (31) Jupally, V. R.; Thrasher, J. G.; Dass, A. Quantized Double Layer Charging of Au<sub>130</sub>(SR)<sub>50</sub> Nanomolecules. *Analyst* **2014**, *139*, 1826–1829.
- (32) Padelford, J. W.; Zhou, M.; Chen, Y.; Jin, R.; Wang, G. Electronic Transitions in Highly Symmetric Au<sub>130</sub> Nanoclusters by Spectroelectrochemistry and Ultrafast Spectroscopy. *J. Phys. Chem. C* **2017**, *121*, 21217–21224.
- (33) Wang, D.; Padelford, J. W.; Ahuja, T.; Wang, G. Transitions in Discrete Absorption Bands of  $Au_{130}$  Clusters upon Stepwise Charging by Spectroelectrochemistry. *ACS Nano* **2015**, *9*, 8344–8351.
- (34) Zhou, M.; Zeng, C.; Chen, Y.; Zhao, S.; Sfeir, M. Y.; Zhu, M.; Jin, R. Evolution from the Plasmon to Exciton State in Ligand-Protected Atomically Precise Gold Nanoparticles. *Nat. Commun.* **2016**, 7, 13240.
- (35) Shabaninezhad, M.; Abuhagr, A.; Sakthivel, N. A.; Kumara, C.; Dass, A.; Kwak, K.; Pyo, K.; Lee, D.; Ramakrishna, G. Ultrafast Electron Dynamics in Thiolate-Protected Plasmonic Gold Clusters: Size and Ligand Effect. *J. Phys. Chem. C* **2019**, *123*, 13344–13353.
- (36) Negishi, Y.; Nakazaki, T.; Malola, S.; Takano, S.; Niihori, Y.; Kurashige, W.; Yamazoe, S.; Tsukuda, T.; Hakkinen, H. A Critical Size for Emergence of Nonbulk Electronic and Geometric Structures in Dodecanethiolate-Protected Au Clusters. *J. Am. Chem. Soc.* **2015**, 137, 1206–1212.
- (37) Hicks, J. F.; Templeton, A. C.; Chen, S.; Sheran, K. M.; Jasti, R.; Murray, R. W.; Debord, J.; Schaaff, T. G.; Whetten, R. L. The Monolayer Thickness Dependence of Quantized Double-Layer Capacitances of Monolayer-Protected Gold Clusters. *Anal. Chem.* 1999, 71, 3703–3711.
- (38) Su, B.; Zhang, M.; Shao, Y.; Girault, H. H. Solvent Effect on Redox Properties of Hexanethiolate Monolayer-Protected Gold Nanoclusters. *J. Phys. Chem. B* **2006**, *110*, 21460–21466.
- (39) Quinn, B. M.; Liljeroth, P.; Ruiz, V.; Laaksonen, T.; Kontturi, K. s. Electrochemical Resolution of 15 Oxidation States for Monolayer Protected Gold Nanoparticles. *J. Am. Chem. Soc.* **2003**, 125, 6644–6645.
- (40) Miles, D. T.; Murray, R. W. Temperature-Dependent Quantized Double Layer Charging of Monolayer-Protected Gold Clusters. *Anal. Chem.* **2003**, *75*, 1251–1257.
- (41) Guo, R.; Georganopoulou, D.; Feldberg, S. W.; Donkers, R.; Murray, R. W. Supporting Electrolyte and Solvent Effects on Single-Electron Double Layer Capacitance Charging of Hexanethiolate-Coated Au<sub>140</sub> Nanoparticles. *Anal. Chem.* **2005**, *77*, 2662–2669.

- (42) Zeng, C.; Chen, Y.; Kirschbaum, K.; Appavoo, K.; Sfeir, M. Y.; Jin, R. Structural Patterns at All Scales in A Nonmetallic Chiral Au<sub>133</sub>(SR)<sub>52</sub> Nanoparticle. *Sci. Adv.* **2015**, *1*, No. e1500045.
- (43) Yan, N.; Xia, N.; Liao, L.; Zhu, M.; Jin, F.; Jin, R.; Wu, Z. Unraveling the Long-Pursued Au<sub>144</sub> Structure by X-Ray Crystallography. *Sci. Adv.* **2018**, *4*, No. eaat7259.
- (44) Chaki, N. K.; Negishi, Y.; Tsunoyama, H.; Shichibu, Y.; Tsukuda, T. Ubiquitous 8 and 29 kDa Gold:Alkanethiolate Cluster Compounds: Mass Spectrometric Determination of Molecular Formulas and Structural Implications. J. Am. Chem. Soc. 2008, 130, 8608–8610.
- (45) Qian, H.; Jin, R. Controlling Nanoparticles with Atomic Precision: The Case of Au<sub>144</sub>(SCH<sub>2</sub>CH<sub>2</sub>Ph)<sub>60</sub>. Nano Lett. **2009**, *9*, 4083–4087.
- (46) Weissker, H. C.; Escobar, H. B.; Thanthirige, V. D.; Kwak, K.; Lee, D.; Ramakrishna, G.; Whetten, R. L.; Lopez-Lozano, X. Information on Quantum States Pervades the Visible Spectrum of the Ubiquitous  $\mathrm{Au}_{144}(\mathrm{SR})_{60}$  Gold Nanocluster. *Nat. Commun.* **2014**, 5. 3785
- (47) Yi, C.; Tofanelli, M. A.; Ackerson, C. J.; Knappenberger, K. L., Jr. Optical Properties and Electronic Energy Relaxation of Metallic Au<sub>144</sub>(SR)<sub>60</sub> Nanoclusters. *J. Am. Chem. Soc.* **2013**, *135*, 18222–18228.
- (48) Byers, C. P.; Hoener, B. S.; Chang, W. S.; Yorulmaz, M.; Link, S.; Landes, C. F. Single-Particle Spectroscopy Reveals Heterogeneity in Electrochemical Tuning of the Localized Surface Plasmon. *J. Phys. Chem. B* **2014**, *118*, 14047–14055.
- (49) Ung, T.; Giersig, M.; Dunstan, D.; Mulvaney, P. Spectroelectrochemistry of Colloidal Silver. *Langmuir* 1997, 13, 1773–1782.
- (50) Wusimanjiang, Y.; Ma, Y.; Lee, M.; Pan, S. Single Gold Nanoparticle Electrode for Electrogenerated Chemiluminescence and Dark Field Scattering Spectroelectrochemistry. *Electrochim. Acta* **2018**, *269*, 291–298.
- (51) Hesari, M.; Ding, Z.; Workentin, M. S. Electrogenerated Chemiluminescence of Monodisperse Au<sub>144</sub>(SC<sub>2</sub>H<sub>4</sub>Ph)<sub>60</sub> Clusters. *Organometallics* **2014**, 33, 4888–4892.